Climate Dynamics
https://doi.org/10.1007/s00382-022-06294-1

The impact of air–sea coupling on the simulation of the hydroclimatic change over Peninsular Florida

Vasubandhu Misra[1,2,3] · **Amit Bhardwaj**[2,3,4]

Received: 15 September 2021 / Accepted: 10 April 2022

Abstract

This study analyzes from a pair of downscaled climate projections over Peninsular Florida (PF) at 10 km grid spacing. One of the downscaled projections corresponds to atmospheric downscaling only with a regional atmospheric model (called the Regional Spectral Model [RSM]). The other projection is related to the coupled ocean–atmosphere Regional Spectral Model-Regional Ocean Model (RSM-ROMS), which downscales both the atmospheric and the oceanic components of the global model simultaneously. The RSM-ROMS shows a better verification of the current climate than the corresponding RSM simulation for some atmospheric variables (precipitation and precipitable water) both over PF and the surrounding oceans. The moisture budget differences between the RSM-ROMS and the RSM simulations for both the current and the future climate show that the differences are larger over the surrounding oceans than over PF. However, RSM-ROMS shows a stronger projected drying over PF than RSM in the mid-twenty-first century. The RSM-ROMS displays a smaller deficit of freshwater over the oceans than RSM because of differences between the simulations in the advection of moisture, divergence of moisture, and moisture flux divergence from transient eddies. The differences in the moisture budget between the simulations over PF are small because of compensatory differences between the divergence of moisture from changes in divergent circulation and the divergence of fluxes from the transient eddies. Our analysis indicates that the air–sea coupling in RSM-ROMS affects the mean gradient of the moisture, the mean divergence, and the transients, which then modulate the advection of moisture, the divergence of moisture, and the convergence of moisture flux, respectively, setting it apart from the RSM simulation.

1 Introduction

This paper describes the differences in the hydroclimate of Peninsular Florida (PF) from two sets of downscaled simulations of global climate model integrations that differ in their representation of air–sea coupling to point out that air-sea interactions in the surrounding oceans play an important role. The efficacy of the dynamic downscaling has been debated for some time on the added value provided from downscaling global climate projections by regional climate models (Castro et al. 2005; Kerr 2011; Pielke and Wilby 2012; Racherla et al. 2012). Although this debate is far from over (e.g., Denis et al. 2002; Di Luca et al. 2012; Laprise 2014; Zhang et al. 2020; Virgilio et al. 2020), there is a growing tendency to raise the horizontal resolution of the global models so that the need for downscaling can be scaled down and critical processes in the climate system can be resolved (Palmer 2014). However, the resources are limited to run very high-resolution global models. It may be noted however that the spatial resolutions for some "select" global model integrations in the Coupled Model Intercomparison Project (CMIP) protocol have increased appreciably to ~ 0.5° or even higher grid spacing in the current CMIP6 (Haarsma et al. 2016; Liang-Liang et al. 2022). But these high resolution global model runs continue to remain a small minority of specialized model runs in the large set of integrations conducted under CMIP. A vast majority in the suite of global models participating in CMIP5 and now in CMIP6 continue to be coarse in resolution ranging between 1° to over 2° grid

---

✉ Vasubandhu Misra
vmisra@fsu.edu

[1] Department of Earth, Ocean and Atmospheric Science, Florida State University, Tallahassee, FL, USA

[2] Center for Ocean-Atmospheric Prediction Studies, Florida State University, Tallahassee, FL, USA

[3] Florida Climate Institute, Florida State University, Tallahassee, FL, USA

[4] India Meteorological Department, Ministry of Earth Sciences, New Delhi, India

spacing in at least the Tier 1 experiments (e.g., Christensen and Boberg 2012; Grose et al. 2020). Therefore, the need to downscale these global model projections for regional-scale application continues.

Recent studies with regional coupled ocean–atmosphere models to downscale global climate model projections have shown promising results (e.g., Li et al. 2014a, b; Misra et al. 2019; Bhardwaj and Misra 2019). They are predicated on the fact that the ocean rectification effect on the overlying atmosphere can have a significant impact on the downscaled integrations. This is especially so when the downscaling is done to a much higher resolution than the global model. For example, PF is one such region that could benefit from coupled downscaling (i.e., downscaling which is inclusive of the coupled evolution of the ocean and overlying atmosphere). Around PF there are prominent mesoscale surface ocean currents (e.g., Loop Current, Florida Current) that are critical to the heat budget of the upper ocean. Therefore, resolving these mesoscale features or using models with horizontal resolutions that permit these features to appear is critical to the regional climate of PF (Misra et al. 2016; Misra and Mishra 2016). These studies, unlike downscaling of the atmospheric component of the climate system, indicate that downscaling the coupled ocean–atmosphere system allows for a more realistic simulation of the regional climate by incorporating coupled air-sea feedbacks. For example, the rectification feedback of the Loop Current eddy permitting climate models on the overlying atmosphere and the upper ocean heat content is well documented (Misra and Mishra 2016; Siqueira and Kirtman 2016; Putrasahan et al. 2017).

The purpose of this study is to give a thorough account of the impact of air–sea coupling on the hydroclimate over PF. Although the focus will be on PF, the impact of the air–sea coupling on the simulations over the surrounding oceans around PF will be carefully examined and related to the changes occurring over PF. This is achieved by comparing the moisture budgets of two sets of downscaled simulations for both the current simulation and the future climate projections from a coupled and an uncoupled to ocean regional atmospheric models. We treat the uncoupled regional atmospheric model as the control integration and the coupled regional ocean–atmosphere model as experiment integration. So, in essence, we first highlight the moisture budget for the current (late twentieth century climate) of the control regional model integration followed by the corresponding differences from the experiment regional model integration. Similarly, we will present the projected change in the moisture budget in the mid-twenty-first century climate of the control regional model integration. This will be supplemented by a discussion of the differences in the moisture budget between the experiment and control regional model integration of the mid-twenty-first century simulation. However, before presenting the comparison of the moisture budgets between the two regional models, we also verify the regional model integrations with corresponding verification of surface meteorological variables (e.g., precipitation, surface temperature, precipitable water).

2 Model description

In this study, we deploy the Regional Spectral Model (RSM) following Juang and Kanamitsu (1994) with further modifications described in Misra et al. (2019). The RSM is used to downscale only the atmospheric component of the climate system, with SST being prescribed to it from the global coupled ocean–atmosphere model that is forcing it at the lateral boundaries. The SSTs are interpolated from the native grid of the ocean component of the global model to the RSM grid. The RSM has been a widely used regional atmospheric model for climate studies (e.g., Misra et al. 2001; Roads 2004; He et al. 2015). The dynamical core of the RSM is based on the spectral method using sine and cosine series to solve the primitive equations (Juang and Kanamitsu 1994). It also uses a spectral damping scheme to reduce climate drift and allows for larger than conventional nesting ratios (Kanamaru and Kanamitsu 2007). The vertical coordinate is based on terrain-following 28 sigma levels with top of the atmosphere at 2 hPa. The physical parameterization schemes used in RSM for this study are outlined in Table 1.

The ocean component of the model is based on the Regional Ocean Modeling System (ROMS; Haidvogel et al. 2000; Shchepetkin and McWilliams 2005). This ocean model is coupled to the RSM to form the RSM-ROMS coupled ocean–atmosphere regional climate model (Li et al. 2012). The coupling does not involve any flux coupler or flux corrections. The two components of the climate system are integrated on identical grid discretization. RSM-ROMS, like the RSM has been extensively used for regional climate studies (Li and Misra 2014a, b; Misra and Mishra 2016; Dai et al. 2018).

Table 1 Physical parameterizations of the RSM

Physical parameterization	References
Shortwave radiation	Chou and Suarez (1994)
Longwave radiation	Chou and Lee (1996)
Clouds (explicit)	Zhao and Carr (1997)
Deep convection	Moorthi and Suarez (1992)
Boundary layer	Ek et al. (2003)
Gravity wave drag	Alpert et al. (1988)
Land surface	Ek et al. (2003)
Shallow convection	Tiedtke (1983)

3 Experiment design and verification data

The dynamic downscaling is conducted for a two 20-year period representing the current climate (1986–2005) and the future climate (2041–2060). The downscaling is conducted for one of the CMIP5 models that contributed to its Tier-1 set of experiments, namely, the Community Climate System Model version 4 (CCSM4; Gent et al. 2011). The nominal resolution of CCSM4 for the atmospheric component was $1.25° \times 0.9°$ and for the oceanic component was $1.11° \times 0.27°$ near the equator and $1.11° \times 0.54°$ poleward of 33° latitude. The 20-year periods of the late 20th and mid-twenty-first century was downscaled using the lateral boundary forcing from the CCSM4 for both the atmosphere and oceanic components at 10 km grid spacing, with the former at 6-h intervals and the latter at monthly interval. For the future projection, we employed the RCP8.5 emission scenario. In the case of RSM, the SST was prescribed from the CCSM4 integrations. We neglect the first year of the RSM-ROMS integration in consideration of spin-up issues of the upper ocean. Therefore, we use the remaining 20 years of the RSM-ROMS and RSM simulations of the current (1986–2005) and future (2041–2060) climate for analysis.

In this study, we use climatological monthly means of January, April, July, and October as representative months for winter, spring, summer, and fall seasons for the moisture budget analysis. The late-twentieth century simulations from the model are verified against the Integrated Multi-satellitE Retrievals for Global Precipitation Mission version 6 precipitation data (IMERG; Huffman et al. 2019). This observed precipitation data is available globally from 2000 to the present at 0.1° grid spacing globally, which incidentally matches with the horizontal resolution of the model integrations of this study. Similarly, the land surface temperature is verified against the Climate Prediction Center global temperature data available at 0.5° grid resolution from 1981 to 2010. Finally, the precipitable water is verified with the NASA Water Vapor Project (Doi: 10.5067/NVAP-M/NVAP_CLIMATE_Total-Precipitable-Water_L3.001), which is available at 1° grid resolution, globally.

4 Methodology of the moisture budget

Moisture budget is one of the most used diagnostics to understand the hydroclimatic projections for a given region (Gleick 1989; Trenberth and Guillemot 1995; Chou and Neelin 2004; Seager et al. 2010). The interest in such studies is to decipher the sources of change that result in the changes to the freshwater flux, which is ultimately so critical to life and other human activities. The moisture budget equation for our model integration can specifically be written as:

$$P - E = P_C + P_L - E = -\frac{\partial W}{\partial t} - \frac{\partial C}{\partial t} - \frac{q_{surf}}{g}\frac{\partial p_{surf}}{\partial t} - \frac{qs_c}{g}\frac{\partial p_{surf}}{\partial t} - \frac{1}{g}\int_{p_{top}}^{p_{surf}} \nabla \cdot \vec{V} q dp - \frac{1}{g}\int_{p_{top}}^{p_{surf}} \nabla \cdot \vec{V} q_c dp \tag{1}$$

where the P–E on the left-hand side of Eq. (1) is the freshwater flux, P is total precipitation that can be decomposed into convective precipitation (P_C) which is handled by the relaxed Arakawa-Schubert scheme (Moorthi and Suarez 1992) and large-scale precipitation (P_L) which is handled by the Zhao and Carr scheme (1997), E is surface evaporation, $W = \frac{1}{g}\int_{p_{top}}^{p_{surf}} q dp$, $C = \frac{1}{g}\int_{p_{top}}^{p_{surf}} q_c dp$, p_{top}, p_{surf} are pressure at the top and at the surface of the atmospheric column, q is specific humidity, q_c is the cloud water mixing ratio, q_{surf} is surface specific humidity, qs_c is surface cloud water mixing ratio, and $\vec{V}$ is the horizontal wind vector.

If we are interested in further understand the roles of the forcing in the moisture budget equation between the time mean quantities and their deviations about this time mean in forcing changes to the freshwater flux, then the variables in Eq. (1) can be divided into time mean (denoted by overbar) and transient (denoted by prime) components and Eq. (1) can be written as:

$$\begin{aligned} \overline{P} - \overline{E} = & -\frac{\partial \overline{W}}{\partial t} - \frac{\partial \overline{C}}{\partial t} - \frac{\overline{q}_{surf}}{g}\left(\frac{\partial \overline{p}_{surf}}{\partial t}\right) \\ & - \frac{\overline{qs_c}}{g}\left(\frac{\partial \overline{p}_{surf}}{\partial t}\right) - \underbrace{\frac{1}{g}\int_{p_{top}}^{p_{surf}} \nabla \cdot \left(\overline{\vec{V}}\,\overline{q}\right) dp}_{Terma_1} \\ & - \underbrace{\frac{1}{g}\int_{p_{top}}^{p_{surf}} \nabla . \left(\overline{\vec{V}}\,\overline{q_c}\right) dp}_{Termb_1} - \underbrace{\frac{1}{g}\int_{p_{top}}^{p_{surf}} \nabla \cdot \left(\overline{\vec{V'} q'}\right) dp}_{Terma_2} \\ & - \underbrace{\frac{1}{g}\int_{p_{top}}^{p_{surf}} \nabla . \left(\overline{\vec{V'} q'_c}\right) dp}_{Termb_2} \\ & - q_{surf}\vec{V}_{surf} \cdot \nabla p_{surf} - qs_c \vec{V}_{surf} \cdot \nabla p_{surf} \end{aligned} \tag{2}$$

where overbar represents monthly mean and prime denotes a departure from the monthly mean (or sub-monthly transients), Terms a_1 and a_2 are water vapor flux divergence contributed by the monthly mean and the transient flow, respectively. Similarly, Terms b_1, and b_2 are the cloud water flux divergence contributed by the monthly and sub-monthly transients, respectively. The last two terms on the right-hand side of Eq. (2) are the surface terms, which have not been decomposed into time mean and transient components. The time-mean divergent flux terms in Eq. (2) can be further decomposed into divergence and advection components as:

$$
\begin{aligned}
\overline{P}-\overline{E} = {} & \overbrace{-\frac{\partial \overline{W}}{\partial t}}^{Term\mathbb{A}} \overbrace{-\frac{\partial \overline{C}}{\partial t}}^{Term\mathbb{B}} \overbrace{-\frac{1}{g}\int_{p_{top}}^{p_{surf}} \overline{\mathrm{q}}\nabla\cdot\overline{\vec{V}}dp}^{Term\mathbb{C}} \overbrace{-\frac{1}{g}\int_{p_{top}}^{p_{surf}} \overline{\vec{V}}\cdot\nabla\overline{q}dp}^{Term\mathbb{D}} \overbrace{-\frac{1}{g}\int_{p_{top}}^{p_{surf}} \nabla\cdot\left(\overline{\vec{V'}q'}\right)dp}^{Term\mathbb{E}} \\
& \overbrace{-\frac{1}{g}\int_{p_{top}}^{p_{surf}} \overline{q}_c\nabla\cdot\overline{\vec{V}}dp}^{Term\mathbb{F}} \overbrace{-\frac{1}{g}\int_{p_{top}}^{p_{surf}} \overline{\vec{V}}\cdot\nabla\overline{q_c}dp}^{Term\mathbb{G}} \overbrace{-\frac{1}{g}\int_{p_{top}}^{p_{surf}} \nabla\cdot\left(\overline{\vec{V'}q'_c}\right)dp}^{Term\mathbb{H}} \\
& \underbrace{-\frac{1}{g}\left(\overline{q}_{surf}\overline{\vec{V}}_{surf}+\overline{q'_{surf}\vec{V'}_{surf}}+\overline{qs}_c\overline{\vec{V}}_{surf}+\overline{qs'_c\vec{V'}_{surf}}\right)\cdot\nabla\overline{\mathrm{p}}_{surf}-\frac{\overline{q}_{surf}}{g}\left(\frac{\partial\overline{p}_{surf}}{\partial t}\right)-\frac{\overline{qs}_c}{g}\left(\frac{\partial\overline{p}_{surf}}{\partial t}\right)}_{Term\mathbb{I}}+\in
\end{aligned}
\tag{3}
$$

In the above equation, we compute each of the terms from the RSM and the RSM-ROMS output (which is available daily at 10 pressure levels [1000, 925, 850, 700, 600, 500, 300, 200, 100, 10] hPa on a 10 km lat/lon grid) and Term $\mathbb{I}$ is obtained as a residual. ϵ in Eq. 3 refers to numerical errors that arise from (1) errors introduced in interpolating the data from model native vertical grids to standardize pressure levels, (2) using spatial and temporal discretization schemes for the diagnosis of Eq. 3 that is different from those used in the numerical models and (3) for not explicitly storing the diffusion tendencies of moisture that also contribute to the budget.

To evaluate the differences in the individual terms of Eq. (3) between the mid-twenty-first century projection and the late twentieth century simulation of the RSM simulation, we follow Seager et al. (2010) to denote

$$\delta(.) = (.)_{21\mathrm{st}} - (.)_{20\mathrm{th}} \tag{4}$$

where subscripts 21st and 20th indicate the values of the various terms of Eq. (3) evaluated from the mid-twenty-first century (2041–2060) and the late-twentieth century (1986–2005) climate simulations. Therefore, operating Eq. (4) on Eq. (3), yields:

$$
\begin{aligned}
\delta\left(\overline{P}-\overline{E}\right) = {} & \overbrace{-\frac{\partial \delta\overline{W}}{\partial t}}^{Term1} \overbrace{-\frac{\partial \delta\overline{C}}{\partial t}}^{Term2} \overbrace{-\frac{1}{g}\int_{p_{top}}^{p_{surf}} \delta\overline{\mathrm{q}}\nabla\cdot\overline{\vec{V}}_{20\mathrm{th}}dp}^{Term3} \overbrace{-\frac{1}{g}\int_{p_{top}}^{p_{surf}} \delta\overline{q}_c\nabla\cdot\overline{\vec{V}}_{20\mathrm{th}}dp}^{Term4} \overbrace{-\frac{1}{g}\int_{p_{top}}^{p_{surf}} \overline{\vec{V}}_{20\mathrm{th}}\cdot\nabla\delta\overline{q}}^{Term5} \\
& \overbrace{-\frac{1}{g}\int_{p_{top}}^{p_{surf}} \overline{\vec{V}}_{20\mathrm{th}}\cdot\nabla\delta\overline{q_c}}^{Term6} \overbrace{-\frac{1}{g}\int_{p_{top}}^{p_{surf}} \overline{q}_{20\mathrm{th}}\nabla\cdot\delta\overline{\vec{V}}}^{Term7} \overbrace{-\frac{1}{g}\int_{p_{top}}^{p_{surf}} \overline{q_c}_{20\mathrm{th}}\nabla\cdot\delta\overline{\vec{V}}}^{Term8} \\
& \overbrace{-\frac{1}{g}\int_{p_{top}}^{p_{top}} \delta\overline{\vec{V}}\cdot\nabla\overline{q}_{20\mathrm{th}}}^{Term9} \overbrace{-\frac{1}{g}\int_{p_{top}}^{p_{top}} \delta\overline{\vec{V}}\cdot\nabla\overline{q_c}_{20\mathrm{th}}}^{Term10} \overbrace{-\frac{1}{g}\int_{p_{top}}^{p_{surf}} \nabla\cdot\delta\left(\overline{\vec{V'}q'}\right)dp}^{Term11} \\
& \overbrace{-\frac{1}{g}\int_{p_{top}}^{p_{surf}} \nabla\cdot\delta\left(\overline{\vec{V'}q'_c}\right)dp}^{Term12} \overbrace{-\frac{1}{g}\int_{p_{top}}^{p_{surf}} \nabla\cdot\left(\delta\overline{\vec{V}}\delta\overline{q}\right)dp}^{Term13} \overbrace{-\frac{1}{g}\int_{p_{top}}^{p_{surf}} \nabla\cdot\left(\delta\overline{\vec{V}}\delta\overline{q_c}\right)dp}^{Term14} \overbrace{-\delta\mathrm{II}}^{Term15}
\end{aligned}
\tag{5}
$$

In Eq. (5), terms involving changes in $\overline{q}$ and $\overline{q_c}$ but not $\vec{\overline{V}}$ are referred as thermodynamic contributors to $(\overline{P}-\overline{E})$ while terms involving changes in $\overline{V}$ but not in $\overline{q}$ and $\overline{q}_c$ in Eq. (5) are called dynamic contributors (Chou et al. 2009; Seager et al. 2010). By this classification then,

$$Thermodynamic\ \ contributors\begin{cases} Terms1,2 \\ Terms3,4,5,6 \end{cases}$$

Some of these thermodynamic terms can be further classified into contributions due to divergence and advection as:

$$Terms3\&4TDIV$$

$$Term5\&6TADV$$

involve covariance and it is difficult to separate them further, meaningfully. In Eq. (5) all the terms are computed separately from the model output with the total of Terms 13, 14, and 15 computed as a residue.

Just as the changes between the late-20th and mid-twenty-first century moisture budget is analyzed; one can also adopt the same procedure to understand the differences in the moisture budget between the simulations from RSM-ROMS and RSM for which, Eq. (4) can be rewritten as:

$$\Delta(.) = (.)_{RSMROMS} - (.)_{RSM} \tag{6}$$

Therefore, like Eq. (5), we can operate Eq. (6) on Eq. (3) to assess the differences in the simulations between RSM-ROMS and RSM for both the late-20th and mid-twenty-first century epochs with the following equation:

$$\begin{aligned}
\Delta\left(\overline{P}-\overline{E}\right) = & -\overbrace{\frac{\partial\overline{\Delta W}}{\partial t}}^{Terma} \overbrace{-\frac{\partial\overline{\Delta C}}{\partial t}}^{Termb} \overbrace{-\frac{1}{g}\int_{p_{top}}^{p_{surf}} \Delta\overline{\mathrm{q}}\nabla\cdot\vec{\overline{V}}_{RSM}dp}^{Termc} \overbrace{-\frac{1}{g}\int_{p_{top}}^{p_{surf}} \Delta\overline{q}_c\nabla\cdot\vec{\overline{V}}_{RSM}dp}^{Termd} \overbrace{-\frac{1}{g}\int_{p_{top}}^{p_{surf}} \vec{\overline{V}}_{RSM}\cdot\nabla\Delta\overline{q}}^{Terme} \\
& \overbrace{-\frac{1}{g}\int_{p_{top}}^{p_{surf}} \vec{\overline{V}}_{RSM}\cdot\nabla\Delta\overline{q_c}}^{Termf} \overbrace{-\frac{1}{g}\int_{p_{top}}^{p_{surf}} \overline{q}_{RSM}\nabla\cdot\Delta\vec{\overline{V}}}^{Termg} \overbrace{-\frac{1}{g}\int_{p_{top}}^{p_{surf}} \overline{q_c}_{RSM}\nabla\cdot\Delta\vec{\overline{V}}}^{Termh} \\
& \overbrace{-\frac{1}{g}\int_{p_{top}}^{p_{top}} \Delta\vec{\overline{V}}\cdot\nabla\overline{q}_{RSM}}^{Termi} \overbrace{-\frac{1}{g}\int_{p_{top}}^{p_{top}} \Delta\vec{\overline{V}}\cdot\nabla\overline{q_c}_{RSM}}^{Termj} \overbrace{-\frac{1}{g}\int_{p_{top}}^{p_{surf}} \nabla\cdot\Delta\left(\overline{\vec{V'}q'}\right)dp}^{Termk} \\
& \overbrace{-\frac{1}{g}\int_{p_{top}}^{p_{surf}} \nabla\cdot\Delta\left(\overline{\vec{V'}q'_c}\right)dp}^{Terml} \overbrace{-\frac{1}{g}\int_{p_{top}}^{p_{surf}} \nabla\cdot\left(\Delta\vec{\overline{V}}\Delta\overline{q}\right)dp}^{Termm} \overbrace{-\frac{1}{g}\int_{p_{top}}^{p_{surf}} \nabla\cdot\left(\Delta\vec{\overline{V}}\Delta\overline{q_c}\right)dp}^{Termn} \overbrace{-\Delta\mathrm{II}}^{Termo}
\end{aligned} \tag{7}$$

where TDIV and TADV are thermodynamic contributions to freshwater flux change from changes in divergence and advection of the moist scalar variables ($\overline{q}$ and $\overline{q}_c$), respectively. And,

$$Dynamic\ contributors\begin{cases} Terms7,8 \\ Terms9,10 \end{cases}$$

And similarly,

$$Terms7\&8DDIV$$

$$Terms9\&10DADV$$

where DDIV and DADV are dynamic contributions to freshwater flux change from changes in divergent and advective circulation components. The transient terms (Terms 11 and 12), other non-linear terms (Terms 13, 14, and 15) in Eq. (5)

5 Results

As noted earlier in the Introduction Section, we first present the validation of the regional model integrations of their current climate simulation in Sect. 5.1. This will then be followed by the detailed analysis of the moisture budget of the current (or the late twentieth century) climate simulation from RSM, which is treated as a control integration in Sect. 5.2. In Sect. 5.3 we draw the comparisons between the moisture budgets of RSM-ROMS (experiment) integration from RSM (control) integration of the current climate simulation. The differences between the mid-twenty-first century and late twentieth century simulation of the RSM integration is presented in Sect. 5.4. In Sect. 5.5 we present the differences in the moisture budgets of the twenty-first century simulation between RSM-ROMS and RSM integrations

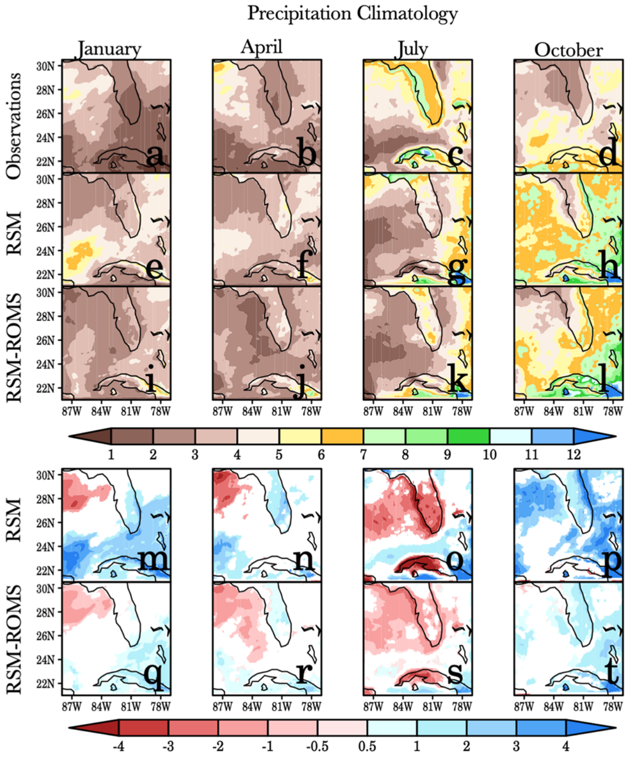

Fig. 1 The **a–d** observed, **e–h** RSM (1986–2005), and **i–l** RSM-ROMS (1986–2005) climatological seasonal cycle of rainfall (mm/day) for **a**, **e**, **i** January, **b**, **f**, **j** April, **c**, **g**, **k** July, and **d**, **h**, **l** October. The corresponding systematic errors (computed as model climatology-observed climatology) of rainfall (mm/day) from **m–p** RSM and **q–t** RSM-ROMS for **m**, **q** January, **n**, **r** April, **o**, **s** July, and **p**, **t** October. Only significant values significant at 5% significance level according to t-test is shaded in **m–t**

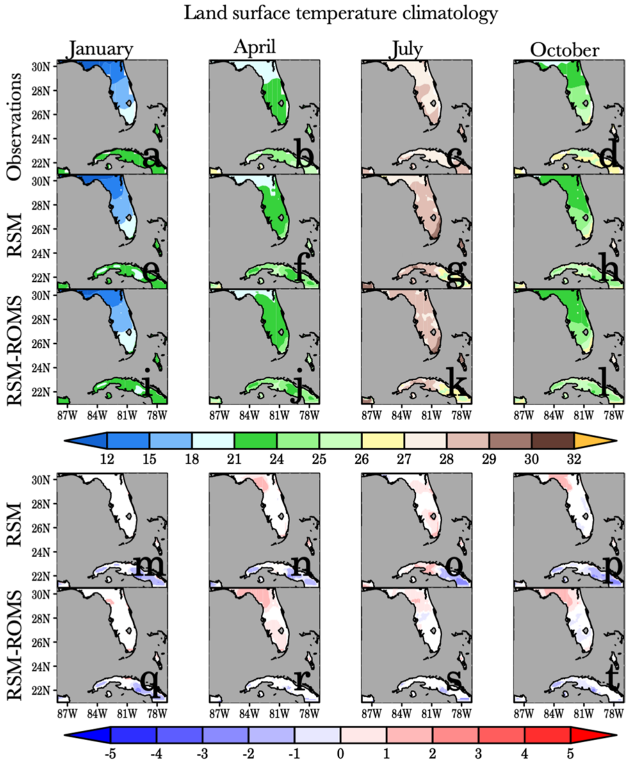

Fig. 2 The **a–d** observed, **e–h** RSM (1986–2005), and **i–l** RSM-ROMS (1986–2005) climatological seasonal cycle of land-surface temperature (°C) for **a**, **e**, **i** January, **b**, **f**, **j** April, **c**, **g**, **k** July, and **d**, **h**, **l** October. The corresponding systematic errors (computed as model climatology-observed climatology) of land-surface temperature (°C) from **m**, **n**, **o**, **p** RSM and **q**, **r**, **s**, **t** RSM-ROMS for **m**, **q** January, **n**, **r** April, **o**, **s** July, and **p**, **t** October. Only significant values significant at 5% significance level according to t-test is shaded in **m–t**

followed by highlighting the differences in the air-sea interactions between the two models in Sect. 5.6.

5.1 Model validation

In Fig. 1 we show the climatological seasonal cycle of rainfall from observations and model simulations for the late-twentieth century period with their corresponding systematic errors (model minus observations). The observed seasonal cycle of rainfall over PF and the surrounding oceans (Fig. 1a–d) is distinct with July appearing as the wettest part of the year with January and April appearing as the driest part of the year when wildfires are frequent (Harrison and Meindl 2001). The RSM simulation of the late twentieth century seems reasonable (Fig. 1e–h), although the wet bias throughout the year is notable (Fig. 1m–p). In fact, October appears to be the wettest part of the year in the RSM simulation (Fig. 1h). In contrast, the RSM-ROMS late twentieth century simulation reduces the wet bias relative to RSM significantly throughout the years (Fig. 1i–l and q–t). It may be noted that RSM-ROMS restores July as the wettest part of the year, unlike RSM.

The seasonal cycle of the land-surface temperature over PF is also equally strong with temperature changes between winter and summer being of the order of 10–15 °C across PF (Fig. 2a–d). The meridional gradient of the surface temperature from south to north PF also shows a strong seasonal cycle with the gradient being strongest in January (Fig. 2a) and weakest in July (Fig. 2c). These seasonal cycle features in the land-surface temperature are simulated in RSM (Fig. 2e–h) and RSM-ROMS (Fig. 2i–l) as well. However, both these model simulations have comparable warm bias throughout the year with insignificant seasonal contrast (Fig. 2m–p and q–t).

The observed climatological precipitable water for the four discrete months also shows a consistent seasonal cycle as the previous two variables, with the precipitable water having a minimum in January and a peak in July (Fig. 3a–d). This is reasonably simulated by the RSM, although the peak in this simulation is seen in October instead of July (Fig. 3e–h). The RSM-ROMS rectifies this bias of the

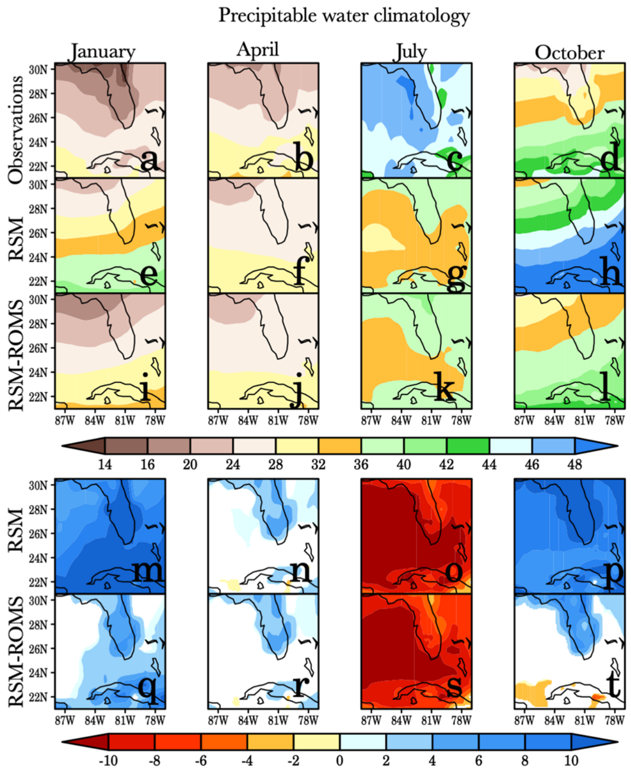

Fig. 3 The **a–d** observed, **e–h** RSM (1986–2005), and **i–l** RSM-ROMS (1986–2005) climatological seasonal cycle of total precipitable water (Kg m^{-2}) for **a**, **e**, **i** January, **b**, **f**, **j** April, **c**, **g**, **k** July, and **d**, **h**, **l** October. The corresponding systematic errors (computed as model climatology-observed climatology) of precipitable water (Kg m^{-2}) from **m–p** RSM and **q–t** RSM-ROMS for **m**, **q** January, **n**, **r** April, **o**, **s** July, and **p**, **t** October. Only significant values significant at 5% significance level according to t-test is shaded in **m–t**

seasonal cycle of the RSM simulation with the peak climatological precipitable water appearing in July. The late twentieth century simulations from both RSM (Fig. 3m–p) and RSM-ROMS (Fig. 3q–t) show similar bias but with different magnitudes. The RSM-ROMS simulation reduces the wet bias in January and October relative to the RSM simulation. In the summer as well, the dry bias of RSM is slightly reduced in RSM-ROMS, while in the spring, the bias is comparable in both model simulations.

In summary, the models do capture the seasonal cycle of precipitation, land-surface temperature, and moisture over the domain of the regional model reasonably well, with significant differences in the simulation between RSM and RSM-ROMS, especially in the winter and summer period of the year. While the models display significant systematic bias there is merit in examining and comparing the moisture budget from these models as one model integration (RSM-ROMS) does better than the other (RSM).

5.2 The moisture budget of the late twentieth century simulation from RSM

As stated earlier, the RSM run is treated as the control integration. The terms on the left and the right-hand sides of Eq. (3) from the late twentieth century simulation from RSM is analyzed in this subsection. The mean freshwater flux ($\overline{P} - \overline{E}$) very clearly displays a seasonal cycle where it is positive in the fall and winter and negative in the spring and summer over PF (Fig. 4a–d; Table 2). Although in the spring (Fig. 4b) and in the summer (Fig. 4c) South Florida and Central Florida displays a near balance between $\overline{P}$ and $\overline{E}$, respectively. However, across PF, the summer season shows a near balance between $\overline{P}$ and $\overline{E}$ (Table 2). Over the oceans, there is a general deficit of the freshwater flux except in the fall season (Fig. 4d) when $\overline{P}$ exceeds $\overline{E}$ near the western and the southern boundaries of the domain, with its antecedents seen in the summer (Fig. 4c).

Figure 4e–h show $Term\mathbb{C}$ ($= -\frac{1}{g}\int_{p_{top}}^{p_{surf}} \overline{q}\nabla \cdot \overline{\overline{V}}dp$;the convergence of moisture) of Eq. (3), for the four months of the year, which is nearly opposite in sign to the freshwater flux over PF. For example, this term in negative in the winter (Fig. 4e) over PF when ($\overline{P} - \overline{E}$) is positive (Fig. 4a; Table 2). Similarly, in spring (Fig. 4f) and summer (Fig. 4g) the convergence of moisture is positive when ($\overline{P} - \overline{E}$) is positive or near zero, respectively. The summer season is the rainy season over PF, when the convergence of moisture assumes significance in the moisture budget (Table 2). In the summer, there is a significant discontinuity in this term over the Gulf of Mexico (Fig. 4g), for which we don't know its source. In the fall, $Term\mathbb{C}$ is positive over South Florida and negative over central and northern parts of PF (Fig. 4h) but is overall positive across PF (Table 2), when ($\overline{P} - \overline{E}$) is positive across PF (Fig. 4d). Over the oceans,$Term\mathbb{C}$ is largely negative and becomes significantly large relative to other months in July.

The advection of moisture, $Term\mathbb{D}$ ($=-\frac{1}{g}\int_{p_{top}}^{p_{surf}} \overline{\overline{V}} \cdot \nabla\overline{q}dp$) in Eq. (3) is shown in Fig. 4i–l, overlaid with 850 hPa winds. Contrary to Term $\mathbb{C}$, this term is positive in the winter (Fig. 4i) and spring (Fig. 4j) while it assumes a negative value in summer (Fig. 4k) and reverts to being positive in fall (Fig. 4l) over PF (Table 2). It is interesting to note that despite these seasonal changes in moisture advection, the climatological 850 hPa circulation field is consistently southwesterly over PF in January, April, and July but becomes easterly in October. Similarly, over the oceans, the advection of moisture is largely positive across all four months, with April showing a widespread positive value. There are however some negative values over the West Florida Shelf in July (Fig. 4k). From comparing Fig. 4e–h with Fig. 4i–l, we can see that the tendencies of the convergence of moisture and advection of moisture largely oppose each

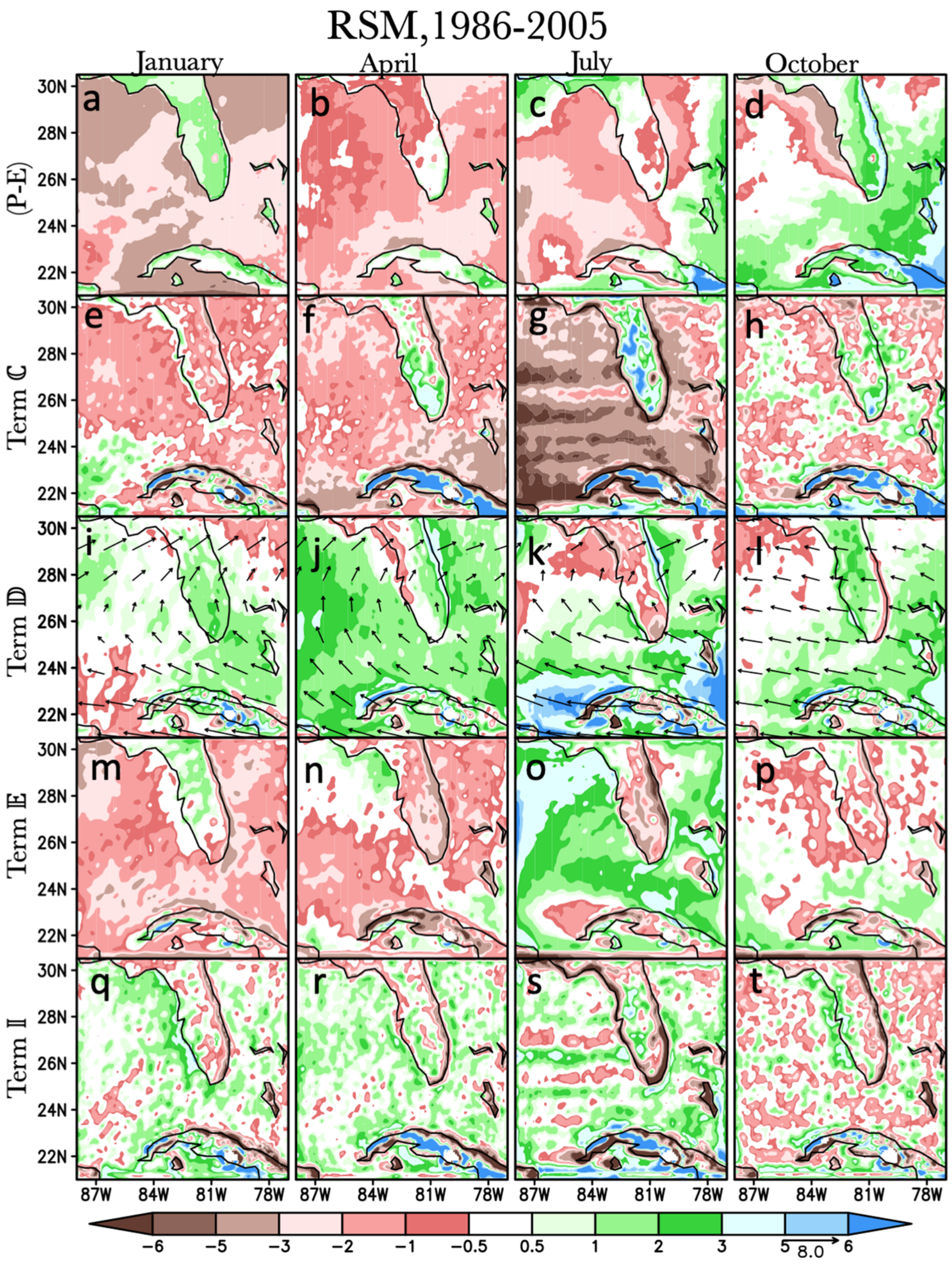

Fig. 4 The terms of the moisture budget (mm/day) from Eq. 3 for the current climate (1986–2005) RSM simulation showing **a**–**d** (P–E) **e**–**h** Term $\mathbb{C}$, **i**–**l** Term $\mathbb{D}$ overlaid with 850 hPa winds (ms^{-1}) **m**–**p** Term $\mathbb{E}$, and **q**–**t** residual Term ($\mathbb{I}$) for **a**, **e**, **i**, **m**, **q** January, **b**, **f**, **j**, **n**, **r** April, **c**, **g**, **k**, **o**, **s** July, and **d**, **h**, **l**, **p**, **t** October

other over PF in winter and summer while reinforcing each other in spring and fall seasons (Table 2).

The moisture tendencies due to convergence of moisture flux by transient eddies,*Term*$\mathbb{E}$ $\left(= -\frac{1}{g}\int_{p_{top}}^{p_{surf}} \nabla \cdot \left(\overline{\vec{V}'q'}\right) dp\right)$ in Eq. (3) is shown in Fig. 4m–p. Here, except in January (Fig. 4m), in all the other three seasons, this tendency is largely negative over PF (Fig. 4n–p; Table 2). Again, except for July (Fig. 4o), *Term*$\mathbb{E}$ is generally negative over the oceans.

The corresponding three terms involving the cloud water mixing ratio, namely, divergence of cloud water mixing ratio, *Term*$\mathbb{F}$ $\left(= -\frac{1}{g}\int_{p_{top}}^{p_{surf}} \overline{q}_c \nabla \cdot \overline{\vec{V}} dp\right.$; Figs. S1a-d [in supplementary material]), advection of cloud water mixing ratio, *Term*$\mathbb{G}$ $\left(= -\frac{1}{g}\int_{p_{top}}^{p_{surf}} \overline{\vec{V}} \cdot \nabla \overline{q_c} dp\right.$;Figs. S1e – h), *Term*$\mathbb{H}$ $\left(= -\frac{1}{g}\int_{p_{top}}^{p_{surf}} \nabla \cdot \left(\overline{\vec{V}'q'_c}\right) dp\right.$; Figs. S1i – l) are comparatively much smaller in magnitude (by at least an order of magnitude or more). The precipitable water tendency, *Term*$\mathbb{A}\left(= -\frac{\partial \overline{W}}{\partial t}\right)$ shown in Figs. (S1m-p) and the integrated column cloud water tendency, *Term*$\mathbb{B}\left(= -\frac{\partial \overline{C}}{\partial t}\right)$ shown in Figs. S1q-t are also extremely small. The *Term*$\mathbb{I}$ of Eq. (3), which is computed as a residue (Fig. 4q–t; Table 2) is comparatively small and spatially incoherent relative to the terms of Eq. (3) shown in the first four rows of Fig. 4.

Table 2 Area average values of the terms of the moisture budget (Eq. 3) over Peninsular Florida (mm/day)

Variable	January		April		July		October	
	RSM	RSM-ROMS	RSM	RSM-ROMS	RSM	RSM-ROMS	RSM	RSM-ROMS
$(\overline{P}-\overline{E})$	1.16	0.70	− 0.31	− 0.44	− 0.01	0.35	2.07	1.95
$-\frac{1}{g}\int_{p_{top}}^{p_{surf}} \overline{q}\nabla.\overrightarrow{\overline{V}}dp$	− 0.9	− 0.84	0.75	1.39	3.45	2.65	1.2	1.06
$-\frac{1}{g}\int_{p_{top}}^{p_{surf}} \overrightarrow{\overline{V}}.\nabla\overline{q}dp$	2.32	0.89	1.64	0.63	− 0.79	− 0.83	2.39	0.81
$-\frac{1}{g}\int_{p_{top}}^{p_{surf}} \nabla\cdot\left(\overline{\overrightarrow{V'}q'}\right)dp$	0.26	− 0.27	− 2.16	− 2.51	− 2.2	− 2.88	− 0.65	− 1.1
$-\frac{1}{g}\int_{p_{top}}^{p_{surf}} \overline{q}_c\nabla.\overrightarrow{\overline{V}}dp \times 100$	− 0.11	− 0.18	− 1.51	− 1.52	− 1.88	− 2.27	− 1.49	− 1.31
$-\frac{1}{g}\int_{p_{top}}^{p_{surf}} \overrightarrow{\overline{V}}.\nabla\overline{q}_c dp \times 10$	0.19	0.21	− 0.37	− 0.86	− 0.1	− 0.14	0.05	− 0.04
$-\frac{1}{g}\int_{p_{top}}^{p_{surf}} \nabla.\left(\overline{\overrightarrow{V'}qc'}\right)dp \times 10$	0.3	− 0.07	− 0.44	− 0.76	− 0.58	− 0.9	0.18	− 0.22
$-\frac{\partial\overline{W}}{\partial t}\times 10,000$	− 0.48	0.03	1.44	0.71	1.05	1.0	0.36	0.01
$-\frac{\partial\overline{C}}{\partial t}\times 100,000$	− 0.51	0.89	0.26	1.3	0.09	0.56	− 0.34	0.08
$-\frac{1}{g}\left(\bar{q}_{surf}\vec{\bar{V}}_{surf}+\overline{q'_{surf}\overrightarrow{V'}_{surf}}+\overline{qc}_{surf}\vec{\bar{V}}_{surf}+\overline{qc'_{surf}\overrightarrow{V'}_{surf}}\right)\cdot \nabla\bar{p}_{surf}-\frac{\bar{q}_{surf}}{g}\left(\frac{\partial\bar{p}_{surf}}{\partial t}\right)-\frac{\overline{qc}_{surf}}{g}\left(\frac{\partial\bar{p}_{surf}}{\partial t}\right)+\in$	− 0.59	0.91	− 0.46	0.23	− 0.42	1.55	− 0.92	1.21

Although, despite the spatial incoherency of the residual term in the winter (Fig. 4q; Table 2) and spring (Fig. 4r; Table 2), it serves as a moisture source over the ocean and as moisture sink over PF. In the summer (Fig. 4s), the residual term shows positive values over PF but along the coasts, it has large negative values that render the average over PF to be negative (Table 2). This residual term also serves to smooth out the discontinuity observed in the divergence of moisture over the Gulf of Mexico (Fig. 4g).

5.3 Differences between the twentieth century simulations of RSM-ROMS and RSM

The comparative differences in the mean freshwater flux $\left(\Delta\left(\overline{P}-\overline{E}\right)\right)$ between RSM-ROMS and RSM (Fig. 5a–d), indicate some large deficits in the latter over the surrounding oceans throughout the year. However, over PF the differences in the freshwater flux between the model simulations are relatively small, especially in the spring and fall seasons (Table 3). The difference in the moisture divergence from changes in humidity (one of the TDIV terms; Term c $=-\frac{1}{g}\int_{p_{top}}^{p_{surf}}\Delta\overline{q}\nabla\cdot\overrightarrow{\overline{V}}_{RSM}dp$ of Eq. 7) in Fig. 5e-h show insignificant differences over the oceans and a very weak relative drying tendency over PF in RSM-ROMS relative to RSM (Table 3). In contrast, the differences in the advection of moisture due to differences in humidity (one of the TADV terms), Term e $(=-\frac{1}{g}\int_{p_{top}}^{p_{surf}}\overrightarrow{\overline{V}}_{RSM}\cdot\nabla\Delta\overline{q})$, shows that there is generally a drying tendency in RSM-ROMS over the oceans relative to RSM, with some strong moistening tendency in the fall appearing over the oceans in the immediate vicinity of PF (Fig. 5i–l; Table 3). Over PF the differences in the tendency of this term is comparatively weak than the oceans but RSM has a stronger moistening tendency than RSM-ROMS (Table 3).

The change in divergence of moisture due to circulation changes (one of the DDIV terms), Term g $(=-\frac{1}{g}\int_{p_{top}}^{p_{surf}}\overline{q}_{RSM}\nabla\cdot\Delta\overrightarrow{\overline{V}})$ in Fig. 5m–p show some large differences both over PF (Table 3) and the surrounding oceans. Over PF, Fig. 5m–p and Table 3 indicate that RSM-ROMS moisten the air column relative to RSM. But over the oceans, in the winter half of the year, RSM-ROMS has a slightly stronger drying tendency (Fig. 5m and n), which shifts to a stronger moistening tendency in the summer half of the year with a strong drying tendency appearing over the West Florida Shelf in the fall (Fig. 5o and p) relative to RSM. The change in the advection of moisture tendency due to circulation changes (one of the DADV terms; Term i $=-\frac{1}{g}\int_{p_{top}}^{p_{top}}\Delta\overrightarrow{\overline{V}}\cdot\nabla\overline{q}_{RSM}$), shows insignificant differences both over the oceans and over PF

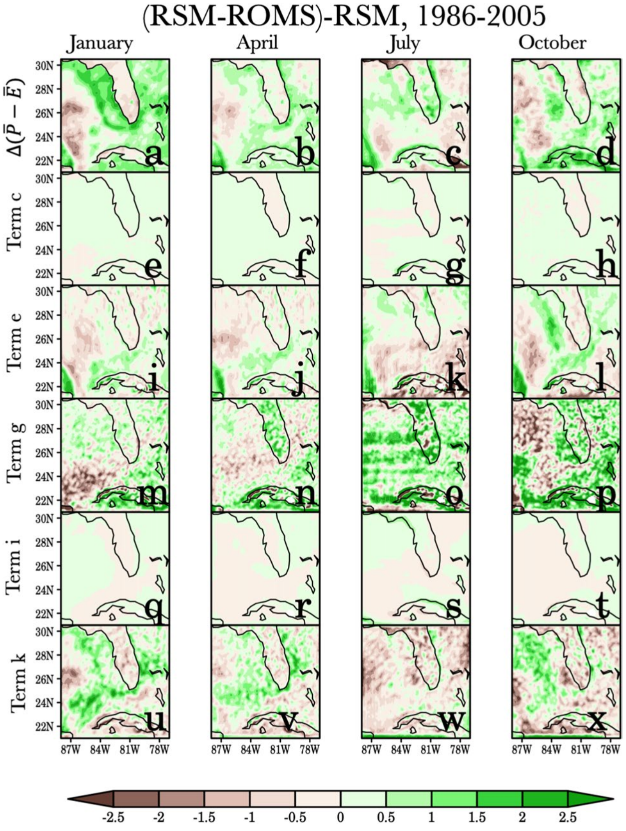

Fig. 5 The differences in the moisture budget between the current climate (1986–2005) simulations from RSM-ROMS and RSM showing **a**–**d** $\Delta(P-E)$, **e**–**h** Term c, **i**–**l** Term e, **m**–**p** Term g, **q**–**t** Term i, and **u**–**x** Term k of Eq. (7) for **a**, **e**, **i**, **m**, **q**, **u** January, **b**, **f**, **j**, **n**, **r**, **v** April, **c**, **g**, **k**, **o**, **s**, **w** July, and **d**, **h**, **l**, **p**, **t**, **x** October. All units are in mm/day

between the two model simulations. The differences in the moisture tendency due to moisture flux divergence from transient eddies (Term k $=-\frac{1}{g}\int_{p_{top}}^{p_{surf}}\nabla\cdot\Delta\left(\overline{\vec{V}'q'}\right)dp$) is relatively large between the two model simulations (Fig. 5u–x; Table 3). Over PF, this term has a stronger drying tendency in RSM-ROMS compared to RSM (Table 3), while over the oceans there is some seasonality in the differences. It may be noted that the remaining terms in the right hand side of Eq. 7 were evaluated and found to be extremely small, which are shown in Fig. S2 (in supplementary material).

In summary, the differences in the moisture budget of the two model simulations are relatively large over the oceans and comparatively small over PF. The small difference over PF is a result of compensatory forcing between divergence of moisture from changes in divergent circulation (Term g of Eq. 7) and the divergence of fluxes from the transient eddies (Term k of Eq. 7). Over the oceans, RSM displays a relative deficit of freshwater flux, which is a result of the combination of the differences arising from Terms e, g, i, and k of Eq. (7). The terms involving cloud water mixing ratio in Eq. (7) were found to be extremely small (see Fig. S2 in supplementary material and Table 3) to account for differences in the moisture budget between the two model simulations.

5.4 Differences between the twenty-first and twentieth century simulations from RSM

The differences in the moisture budget terms, following Eq. (5) from the RSM simulations between the future (2041–2060) and the current (1986–2005) climate simulations are shown in Fig. 6. The differences in the freshwater flux ($\delta(\overline{P}-\overline{E})$) in Fig. 6a–d indicates that in the future climate, there is a relative deficit in spring and summer over PF and the surrounding oceans while in the other two seasons the deficit is less homogenous in the domain, with the winter (Fig. 6a) showing excess over the oceans. The future changes in the divergence of the moisture owing to changes in moisture (Term 3 of Eq. 5 $=-\frac{1}{g}\int_{p_{top}}^{p_{surf}}\delta\overline{q}\nabla\cdot\overline{\vec{V}}_{RSM}dp$) is relatively very small (Fig. 6e–h). In contrast, the changes in the tendency due to advection of moisture owing to changes in moisture (Term 5 of Eq. 5 $=-\frac{1}{g}\int_{p_{top}}^{p_{surf}}\overline{\vec{V}}_{RSM}\cdot\nabla\delta\overline{q}$; Fig. 6i–l) is nearly of the opposite sign to the changes in freshwater flux. For example, the drying tendencies in the winter (Fig. 6i) and in the fall (Fig. 6l), and the moistening tendencies in the spring (Fig. 6j) and summer (Fig. 6k) of this term over PF and the oceans are opposite to the corresponding changes in the freshwater flux (Fig. 6a–d). Figure 6m–p, show the future change in the tendencies due to divergence of moisture from changes in the divergent circulation (Term 7 of Eq. 5 $=-\frac{1}{g}\int_{p_{top}}^{p_{surf}}\overline{q}_{RSM}\nabla\cdot\delta\overline{\vec{V}}$), which indicate a very strong drying tendency along the eastern coast and northern PF and over the oceans in the summer, while in the rest of the year there is some moistening tendency over PF. In the winter, there is a more homogenous distribution of moistening tendency in the domain due to Term 7 (Fig. 6m) that shifts to a drying tendency in the spring over the oceans (Fig. 6n). In the fall, the strong drying tendency from the summer continues but shifts to the southern and western parts of the domain (Fig. 6p). The drying tendency (with the exception of along the western coast of PF) from changes in advection of moisture due to circulation changes (Term 9 of Eq. 5 $=-\frac{1}{g}\int_{p_{top}}^{p_{top}}\delta\overline{\vec{V}}\cdot\nabla\overline{q}_{RSM}$), are far smoother and more homogenous (Fig. 6q–t) but slightly weaker than Term 5. The changes in the moisture flux convergence due to transient eddies (Term 11 of

Table 3 Area averaged differences over PF in the moisture budget terms (mm/day) between RSM-ROMS and RSM in the late 20th and the mid-twenty-first century simulations

Terms	January		April		July		October	
	20th	21st	20th	21st	20th	21st	20th	21st
$\Delta(\overline{P}-\overline{E})$	– 0.46	– 0.4	– 0.1	0	0.36	– 0.39	– 0.13	0.08
$-\frac{1}{g}\int_{p_{top}}^{p_{surf}}\Delta\overline{\mathrm{q}}\nabla\cdot\overrightarrow{\overline{V}}_{RSM}dp$	0.04	0.03	– 0.11	– 0.12	– 0.13	– 0.17	– 0.04	– 0.07
$-\frac{1}{g}\int_{p_{top}}^{p_{surf}}\overrightarrow{\overline{V}}_{RSM}\cdot\nabla\Delta\overline{q}$	– 0.14	– 0.13	– 0.06	– 0.15	– 0.02	– 0.19	– 0.24	– 0.29
$-\frac{1}{g}\int_{p_{top}}^{p_{surf}}\overline{q}_{RSM}\nabla\cdot\Delta\overrightarrow{\overline{V}}$	0.01	0.28	0.78	0.75	1.06	0.85	0.47	0.99
$-\frac{1}{g}\int_{p_{top}}^{p_{top}}\Delta\overrightarrow{\overline{V}}\cdot\nabla\overline{q}_{RSM}$	– 0.04	0.04	0.02	0.03	0.04	0.07	0.01	– 0.01
$-\frac{1}{g}\int_{p_{top}}^{p_{surf}}\nabla\cdot\Delta\left(\overline{\overrightarrow{V'}q'}\right)dp$	– 0.53	– 0.74	– 0.35	– 0.29	– 0.68	– 0.51	– 0.45	– 0.55
$-\frac{1}{g}\int_{p_{top}}^{p_{surf}}\Delta\overline{q}_c\nabla\cdot\overrightarrow{\overline{V}}_{RSM}dp\times 100$	0.11	0.1	0.15	0.22	– 0.44	– 0.27	0.09	0
$-\frac{1}{g}\int_{p_{top}}^{p_{surf}}\overrightarrow{\overline{V}}_{RSM}\cdot\nabla\Delta\overline{q}_c\times 10$	0	– 0.18	– 0.36	0.09	– 0.03	– 0.02	– 0.05	– 0.21
$-\frac{1}{g}\int_{p_{top}}^{p_{surf}}\overline{q}_{cRSM}\nabla\cdot\Delta\overrightarrow{\overline{V}}\times 100$	– 0.27	– 0.35	– 0.16	– 0.28	0.15	0.06	0.16	0.09
$-\frac{1}{g}\int_{p_{top}}^{p_{top}}\Delta\overrightarrow{\overline{V}}\cdot\nabla\overline{q}_{cRSM}\times 100$	– 0.08	– 0.05	– 0.01	0.01	0.03	0.05	0.01	0
$-\frac{1}{g}\int_{p_{top}}^{p_{surf}}\nabla\cdot\Delta\left(\overline{\overrightarrow{V'}q'_c}\right)dp\times 10$	– 0.36	– 0.53	– 0.32	– 0.26	– 0.41	– 0.19	– 0.41	– 0.46
$\left[-\frac{\partial\overline{\delta W}}{\partial t}-\frac{\partial\overline{\delta C}}{\partial t}-\frac{1}{g}\int_{p_{top}}^{p_{surf}}\nabla\cdot\left(\Delta\overrightarrow{\overline{V}}\Delta\overline{q}\right)dp-\frac{1}{g}\int_{p_{top}}^{p_{surf}}\nabla\cdot\left(\Delta\overrightarrow{\overline{V}}\Delta\overline{q}_c\right)dp-\Delta R\right]\times 10$	0.2	0.23	– 0.29	– 0.16	0.17	– 0.35	0.17	0.06

Eq. 5 $=-\frac{1}{g}\int_{p_{top}}^{p_{surf}}\nabla\cdot\delta\left(\overline{\overrightarrow{V'}q'}\right)dp$) show a moistening tendency over PF in the winter (Fig. 6u) that reverts to drying tendency in the spring (Fig. 6v) and summer (Fig. 6w), which again changes back to moistening tendency in the fall (Fig. 6x). Over the oceans, this term generally shows a moistening tendency throughout the year except for summer, when the oceans in the southern part of the domain display a drying tendency. Once again, the terms involving the cloud water mixing ratio in Eq. 5 are comparatively very small (see Fig. S3 in the supplementary material).

In summary, Fig. 6 shows that the future peak deficit of freshwater flux over PF in the summer is in large part arising from the dynamic contribution of the circulation changes leading to stronger drying tendency from Term 7 (one of the DDIV terms) and Term 9 (one of the DADV terms), with additional drying tendency from the moisture divergence due to transient eddies. The thermodynamic contribution of Term 5 (one of the TADV terms) serves as a moistening tendency to weaken the overall drying tendency in the summer.

5.5 Differences between the twenty-first century simulations of RSM-ROMS and RSM

The differences of the twenty-first century simulations of RSM-ROMS and RSM are again evaluated through Eq. (7) and displayed in Fig. 7. The contrast in the freshwater flux differences between January (Fig. 7a) and July (Fig. 7c) is most apparent, with the former showing an excess while the latter showing a deficit in RSM-ROMS relative to RSM over the oceans. Over PF the differences between the simulations are weak but show a relative deficit in RSM-ROMS with a peak difference in the winter and summer (Table 3). These differences are largely sustained by differences due to

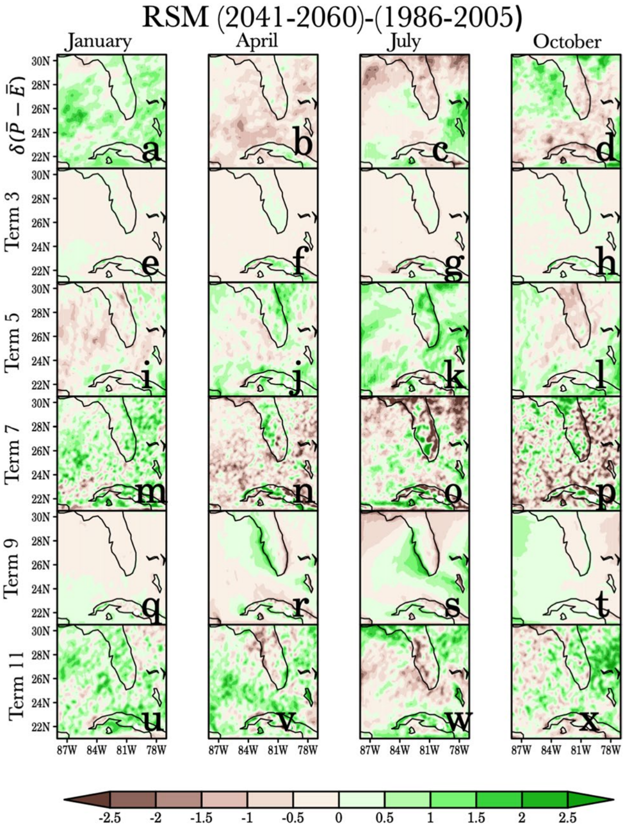

Fig. 6 The differences in the moisture budget between the future climate (2041–2060) and the current climate (1986–2005) simulations from RSM showing **a–d** ($\delta(\overline{P}-\overline{E})$), **e–h** Term 3, **i–l** Term 5, **m–p** Term 7, **q–t** Term 9, and **u–x** Term 11 of Eq. (5) for **a**, **e**, **i**, **m**, **q**, **u** January, **b**, **f**, **j**, **n**, **r**, **v** April, **c**, **g**, **k**, **o**, **s**, **w** July, and **d**, **h**, **l**, **p**, **t**, **x** October. All units are in mm/day

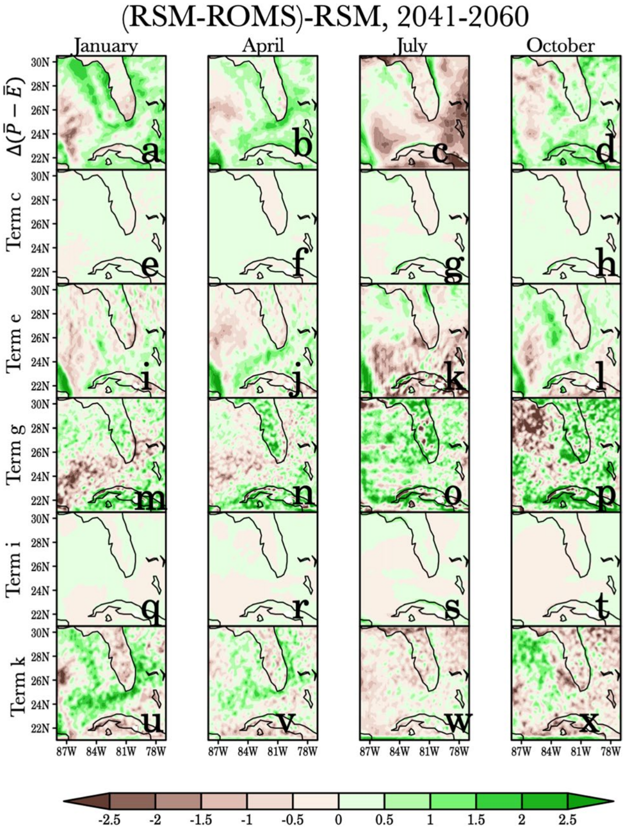

Fig. 7 The differences in the moisture budget between the future climate (2041–2060) simulations from RSM-ROMS and RSM showing **a–d** $\Delta(P-E)$, **e–h** Term c, **i–l** Term e, **m–p** Term g, **q–t** Term i, and **u–x** Term k of Eq. (7) for **a**, **e**, **i**, **m**, **q**, **u** January, **b**, **f**, **j**, **n**, **r**, **v** April, **c**, **g**, **k**, **o**, **s**, **w** July, and **d**, **h**, **l**, **p**, **t**, **x** October. All units are in mm/day

drying tendencies from moisture advection due to changes in moisture (Term e of Eq. 7; Fig. 7i–l) and moisture flux divergence from transient eddies (Term k of Eq. 7; Fig. 7u–x) with counteracting moistening tendency from the divergence of moisture due to changes in divergent circulation (Term g of Eq. 7). The differences in the tendencies due to divergence of moisture from changes in moisture (Term c of Eq. 7; Fig. 7e–h and Table 3) and advection of moisture due to changes in winds (Term i of Eq. 7; Fig. 7u–x and Table 3) are comparatively very small. The terms involving cloud water mixing ratio continue to remain very small in their differences between the two simulations (Fig. S4 in the supplementary material).

These differences indicate that the air–sea coupling in RSM-ROMS affects the mean gradient of the moisture, the mean divergence, and the transients, which then modulates the advection of moisture, the divergence of moisture, and convergence of moisture flux, respectively.

5.6 The role of air-sea coupling

The differences in the moisture budget between RSM and RSM-ROMS is obviously on account of the air–sea coupling because that is one factor that is different between the two model integrations. But what aspect of this air–sea coupling could we isolate this impact to? This is the question we will focus on in this sub-section. There are many ways of examining air-sea coupling. One way to diagnose this coupling is to find the remote influence of SST through atmospheric bridges (Lau and Nath 1996; Klein et al. 1999; Alexander et al. 2002). Another way to diagnose the air–sea coupling is through regional process studies relating atmospheric variations with oceanic variations (e.g., Loschnigg and Webster 2000; Webster 2006; Misra and Mishra 2016). The third way is by diagnosing the local air-sea interactions (e.g., Wang et al. 2005; Wu et al. 2006). In fact, Wang et al. (2005) diagnosed the local rainfall-SST correlations in global climate models over southeast Asia to suggest that the two-tier approach of prescribing SST to global atmospheric models is inadequate to simulate the monsoon variability over the region. We have adopted a similar approach in this paper to diagnose the differences in the local-air sea interaction between RSM and RSM-ROMS.

The local air-sea interaction is manifested in the correlations between atmospheric variables and SST (Frankignoul and Hasselmann 1977; Frankignoul 1985; Barsugli and Battisti 1998; von Storch 2000; Wu et al. 2006, 2008). For example, the lag-lead correlation between rainfall and SST can reveal which component of the climate is forcing and which component of the climate is responding to the forcing (Wu et al. 2006). For instance, a positive correlation between SST and rainfall, when SST leads rainfall would suggest that the SST is forcing the atmosphere. Similarly, a negative correlation between SST and rainfall, when SST lags rainfall implies that the atmosphere is forcing the SST. A positive simultaneous correlation (i.e., at zero lag) between rainfall and SST would suggest, for example, that warm SST anomaly enhance rainfall, which is usually through enhanced evaporation and low-level moisture convergence (Wu et al. 2006). In other words, such positive correlations at zero lag indicate SST forcing of the atmosphere dominates. Wu et al. (2008) showed lag-lead correlations between daily SST and rainfall to display the sub-seasonal variations of air-sea interactions in the northern Indian Ocean to isolate the role of air-sea interactions on transient systems. As they suggest, these correlations are transient since the air–sea coupling at these sub-seasonal scales is a function of the duration and intensity of the system over the ocean.

The nonmonotonic SST–precipitation relationship is a result of the complex interplay between SST, circulation, and precipitation (Waliser and Graham 1993; Zhang 1993; Lau et al. 1997). Therefore, the SST–precipitation relationship can be interpreted as an integrated, coupled response of the thermodynamic and the kinematic fields. Hence, the differences in this metric of the local air-sea relationship can be used to reconcile the differences we observe in the moisture budget of the two model simulations of both the current and future climate.

The transient air–sea coupling feature in RSM-ROMS is best illustrated in the correlations shown between rainfall and SST from the current climate integrations for the four seasons in Fig. 8. Figure 8 shows the mean correlations (averaged over the 20 years) at zero lag, 2 days lag and 2 days lead between rainfall and SST from the 20 year integration of RSM-ROMS. In January, the SST-rainfall correlations are weak at all lead/lag (Fig. 8a–c). In regions where strong correlations do appear in Fig. 8a–c, it is suggestive of coupled air-sea feedbacks. For example, off the central west coast of Florida, the negative correlation when SST is lagging rainfall by 2 days in Fig. 8b suggests that the atmosphere is forcing the SST. In contrast, the positive correlations when SST is leading rainfall by 2 days in Fig. 8c suggests that SST is forcing the rainfall. In comparison, the RSM integrations show weak air-sea feedback in January (Fig. 9a–c).

Similarly, in April, July, and October there is evidence of robust air-sea interaction in RSM-ROMS (Fig. 8d–l) which is much weaker than non-existent in RSM (Fig. 9d–l). However, RSM-ROMS displays significant regions of air-sea feedback interspersed with insignificant regions of air-sea interaction, which suggests the nature of the high frequency variations. Unlike the tropical Indian Ocean where the intraseasonal oscillations can provide spatio-temporal coherency in the air-sea feedback (e.g., Wu et al. 2008), the oceans around PF are not impacted by the sub-seasonal oscillations but are impacted by much higher frequency transient weather.

It is interesting to note in Fig. 8, that all seasons show similar robust air-sea interactions, suggestive of the strong

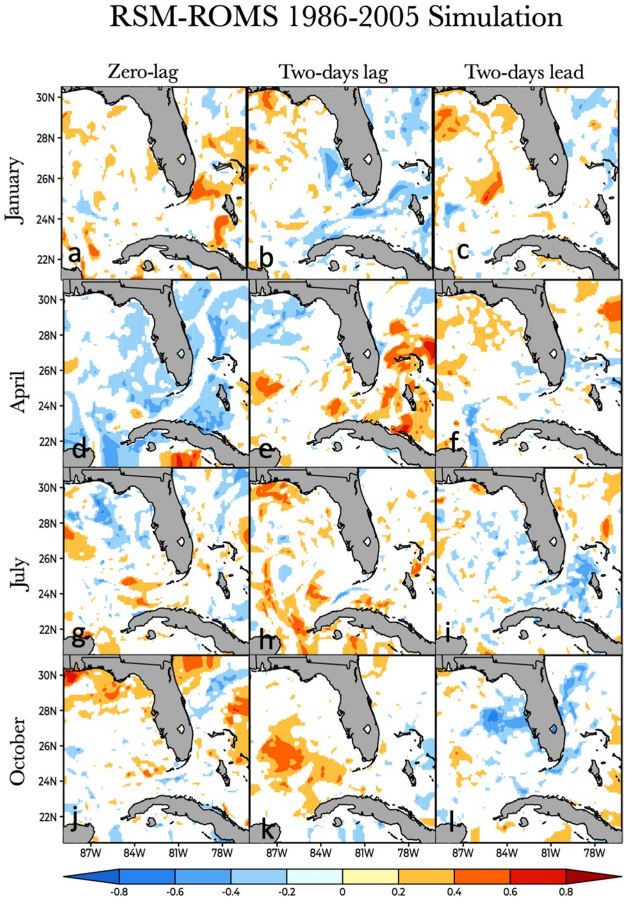

Fig. 8 The local mean correlation between SST and rainfall for **a**–**c** January, **d**–**f** April, **g**–**i** July, and **j**–**l** October at **a**, **d**, **g**, **j** zero-lag, **b**, **e**, **h**, **k** at two-day lag with SST lagging rainfall, and **c**, **f**, **i**, **l** at the two-day lead with SST leading rainfall from the RSM-ROMS, 1986–2005 integration. Only significant correlations at 90% confidence interval according to the two-tailed t-test are shaded

air–sea coupling prevalent in the transient rain bearing systems of the region. This relationship is easily conceivable for example, from the passage of winter storms passing over the Gulf of Mexico, which show very strong air-sea interactions (Bosart et al. 1996; Dickinson et al. 1997). Similarly, tropical cyclones are also known to show robust air-sea interactions in the Gulf of Mexico in the boreal summer and fall seasons (Mainelli-Huber 2000; Shay and Uhlhorn 2008). But many of the transient eddies in the region are not necessarily such extreme events. In fact, many of the transient eddies as the definition suggests, are just departures from the time-mean flow, which are displaying in aggregate a strong rainfall-SST relationship in RSM-ROMS (Fig. 8).

In contrast, the correlations at these short lead and lag between rainfall and SST are significantly smaller in magnitude in the RSM integration (Fig. 9) compared to the RSM-ROMS integrations (Fig. 8). This difference in air-sea interaction between the two models at short time scales is consistent with the domination of the differences in the moisture tendency due to moisture flux divergence from transient eddies between the two models.

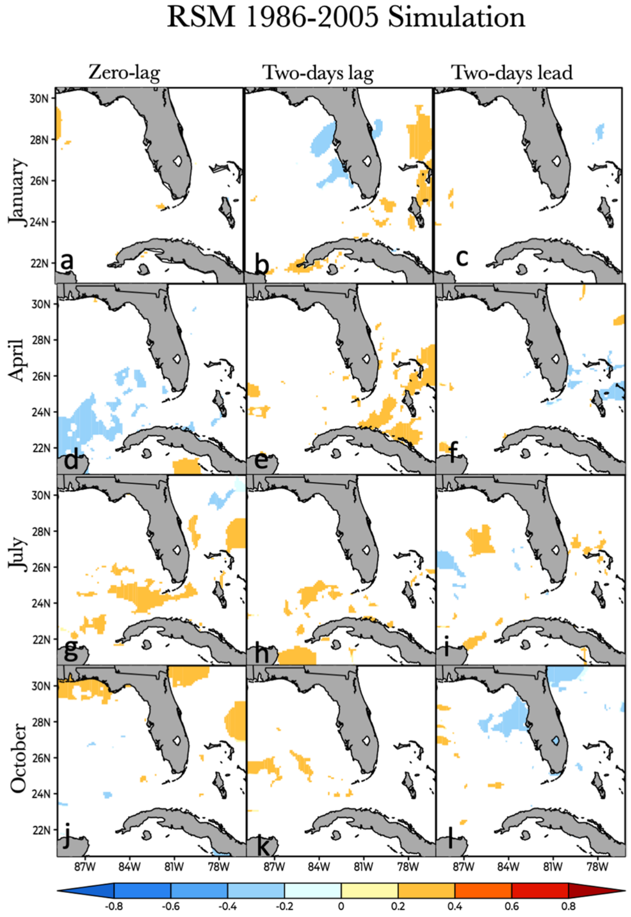

Fig. 9 The local mean correlation between SST and rainfall for **a–c** January, **d–f** April, **g–i** July, and **j–l** October at **a**, **d**, **g**, **j** zero-lag, **b**, **e**, **h**, **k** at two-day lag with SST lagging rainfall, and **c**, **f**, **i**, **l** at the two-day lead with SST leading rainfall from the RSM, 1986–2005 integration. Only significant correlations at 90% confidence interval according to the two-tailed t-test are shaded

6 Conclusions

In this study, a detailed moisture budget analysis has been conducted with unique sets of regional climate simulations centered over PF for the current (1986–2005) and future (2041–2060) climate. They are unique from the sense of their unprecedented horizontal resolution of 10 km grid spacing conducted both for the atmospheric and the oceanic components in the case of RSM-ROMS for this region. The comparison of the atmospheric moisture budgets between the RSM-ROMS and the RSM simulations both for the current and the future climate provides a distinct perspective on the impact of air–sea coupling on hydroclimate projections over PF and the surrounding oceans.

The coupled model, RSM-ROMS, shows some distinctive improvement in the seasonality of the precipitation and precipitable water over PF relative to RSM. For example, the wet bias displayed by RSM throughout the year is significantly reduced in RSM-ROMS. In light of the previous studies, which have highlighted that the seasonal cycle of the neighboring ocean is strongly tied to the seasonal cycle of the hydroclimate over PF (Misra and Mishra 2016; Misra et al. 2017), these results of RSM-ROMS show a better seasonal simulation of the hydroclimate of PF than RSM is not surprising. In this study, we pursue these differences to diagnose the moisture budget between the model simulations both for the current and future climate projections.

The seasonal cycle of the moisture budget of the RSM for the current climate reveals that the freshwater flux ($\overline{P}-\overline{E}$) is positive in January and October and negative in April and July over PF, while over the oceans they are mostly negative except in October when they turn positive in parts of the ocean south and east of PF. This is largely sustained by the advection of moisture by the mean flow and convergence of moisture by the transient flow and opposed by the convergence of moisture by the mean flow. The moisture budget in RSM-ROMS shows a similar seasonality as RSM but the differences are larger over oceans than in PF. The RSM-ROMS displays a smaller deficit of freshwater over the oceans than RSM because of differences between the simulations in the advection of moisture (from differences in moisture-thermodynamic contribution) and divergence of moisture (from differences in divergence-dynamic contribution) and moisture flux divergence from the transient eddies. The differences in the moisture budget between the simulations over PF are small because of compensatory differences between the divergence of moisture from changes in divergent circulation and the divergence of fluxes from the transient eddies.

The projected change in the moisture budget of the RSM simulation for the mid-twenty-first century suggests that the differences in the freshwater flux in the winter is small while in the summer there is a projection for a significant deficit. This deficit arises from stronger drying tendencies in the future from divergence of moisture arising from changes in divergence (dynamic contributor), advection of moisture arising from changes in winds (dynamic contributor) and moisture flux divergence due to transient eddies. These drying tendencies of the future climate are tempered by the moistening tendency of advection of moisture from changes in moisture (thermodynamic contributor). The RSM-ROMS further exacerbates the projected drying over PF and the surrounding oceans in the summer while moistening the neighboring oceans in the winter (with the drying tendency maintained, albeit, weaker over PF). Further analysis of these differences indicates that the air–sea coupling engendered by the transients in RSM-ROMS affects the mean gradient of the moisture, the mean divergence, and the transients, which then modulate the advection of moisture, the divergence of moisture and the convergence of moisture flux, respectively, setting it apart from the RSM simulation. It may be noted that these differences between RSM-ROMS and RSM simulations of the future climate appear in the same terms of the moisture budget equation as that in the current climate simulation.

Our analysis of these differences in the moisture budgets between the RSM and RSM-ROMS shows that they could be isolated to the different manifestations of the air-sea interactions of the transient rain bearing systems in the two models. Our study shows that RSM-ROMS displays a stronger rainfall-SST relationship for these transient systems than RSM across the year. This rainfall-SST relationship is regarded as an integrated atmospheric response (of both kinematic and thermodynamic variables). Therefore, the differences in the local air-sea relationship can be used to reconcile the differences we observe in the moisture budget of the two model simulations of both the current and future climate. We, therefore, conclude from this work that the inclusion of air–sea coupling in the modeling framework to study the regional climate of PF is important.

Indeed, these conclusions of the moisture budget over PF is specific to the two sets of regional climate simulations of the current and the future climate analyzed in this study. We have not considered the uncertainty of the models, emission scenarios, and internal variability, which would likely make the conclusions more assertive. However, our intention was to assess the impact of air–sea coupling on the moisture budget and use this study to motivate the expansion of the work to downscale more global models and emission scenarios with their ensemble members. Our results suggest that the impact of air–sea coupling is non-trivial and affects the mean divergent circulation, mean gradients of humidity, and the transient eddies that have an implication on the hydroclimate of PF and the surrounding oceans.

Supplementary Information The online version contains supplementary material available at https://doi.org/10.1007/s00382-022-06294-1.

Acknowledgements This work was supported by grants from NASA grants 80NSSC19K1199 and NNX17AG72G and the South Florida Water Management District (PO 039231). The supercomputing facility provided by XSEDE under grant number ATM10010 was used in addition to the Florida State University High Performance Computing Cluster to complete the model integrations used in this study. CPC Global Temperature data is provided by the NOAA/OAR/ESRL PSL, Boulder, Colorado, USA, from their Web site at https://psl.noaa.gov/.

Data availability statement The validation datasets are available from public repositories cited in the text and in the acknowledgement. The authors were unable to find a valid data repository for the model data used in this study. These data are available from the first author, vmisra@fsu.edu upon request.

References

Alexander MA, Bladé I, Newman M, Lanzante JR, Lau N-C, Scott JD (2002) The atmospheric bridge: the influence of ENSO teleconnections on air-sea interaction over the global oceans. J Clim 15:2205–2231. https://doi.org/10.1175/1520-0442(2002)015%3c2205:TABTIO%3e2.0.CO;2

Alpert JC, Kanamitsu M, Caplan PM, Sela JG, White G, Kalnay E (1988) Mountain induced gravity wave drag parameterization in the NMC medium-range forecast model. In: Proc. 8th Conf. on Numerical Weather Prediction, Baltimore, MD, Amer. Meteor. Soc., pp 726–733

Barsugli JJ, Battisti DS (1998) The basic effects of atmosphere-ocean thermal coupling on midlatitude variability. J Atmos Sci 55:477–493

Bhardwaj A, Misra V (2019) The role of air-sea coupling in the downscaled hydroclimate projection over Peninsular Florida and the West Florida Shelf. Clim Dyn. https://doi.org/10.1007/s00382-019-04669-S

Bosart LF, Hakim GJ, Tyle KR, Bedrick MA, Dickinson MJ, Schultz DM (1996) Large-scale antecedent conditions associated with the 12–14 March 1993 cyclone ("Superstorm'93") over eastern North America. Mon Wea Rev 124:1865–1891

Castro CL, Pielke RA Sr, Leoncini G (2005) Dynamical downscaling: assessment of value retained and added using the Regional Atmospheric Modeling System (RAMS). J Geophys Res 110:D05108. https://doi.org/10.1029/2004/D004721

Chou M-D, Lee K-T (1996) Parameterizations for the absorption of solar radiation by water vapor and ozone. J Atmos Sci 53:1203–1208

Chou C, Neelin JD (2004) Mechanisms of global warming impacts on regional tropical precipitation. J Clim 17:2688–2701. https://doi.org/10.1175/1520-0442(2004)017%3c2688:MOGWIO%3e2.0.CO;2

Chou C, Neelin JD, Chen C-A, Tu J-Y (2009) Evaluating the "rich-get-richer" mechanism in tropical precipitation change under global warming. J Clim 22(8):1982–2005. https://doi.org/10.1175/2008JCLI2471.1

Chou MD, Suarez MJ (1994) An efficient thermal infrared radiation parameterization for use in general circulation models. In: National Aeronautics and Space Administration, Goddard Space Flight Center. tech. memo, vol 104606, p 85

Christensen JH, Boberg F (2012) Temperature dependent climate projection deficiencies in CMIP5 models. Geophys Res Lett. https://doi.org/10.1029/2012GL053650

Dai Y, Li H, Sun L (2018) The simulation of East Asian summer monsoon precipitation with a regional ocean–atmosphere coupled model. J Geophys Res Atmos. https://doi.org/10.1029/2018JD028541

Denis B, Laprise R, Caya D, Cote J (2002) Downscaling ability of one-way nested regional climate models. The BigBrother Experiment. Clim Dyn 18:627–646

Di Luca A, de Elía R, Laprise R (2012) Potential for added value in precipitation simulated by high-resolution nested Regional Climate Models and observations. Clim Dyn 38(5–6):1229–1247. https://doi.org/10.1007/s00382-011-1068-3

Dickinson MJ et al (1997) The March 1993 superstorm cyclogenesis: incipient phase synoptic and convective scale flow interaction and model performance. Mon Wea Rev 125:3041–3072

Ek MB, Mitchell KE, Lin Y, Rogers E, Grunmann P, Koren V, Gayno G, Tarpley JD (2003) Implementation of Noah land surface model advances in the National Centers for Environmental Prediction operational mesoscale Eta model. J Geophys Res Atmos 108:D22. https://doi.org/10.1029/2002JD003296

Frankignoul C (1985) Sea surface temperature anomalies, planetary waves, and air-sea feedbacks in the middle latitudes. Rev Geophys 23:357–390

Frankignoul C, Hasselmann K (1977) Stochastic climate models. II: application to sea-surface temperature anomalies. Tellus 29:284–305

Gent PR, Danabasoglu G, Donner LJ, Holland MM, Hunke EC, Jayne SR, Lawrence DM, Neale RB, Rasch PJ, Vertenstein M, Worley PH (2011) The community climate system model version 4. J Clim 24(19):4973–4991. https://doi.org/10.1175/2011JCLI4083.1

Gleick PH (1989) Climate change, hydrology, and water resources. Rev Geophys. https://doi.org/10.1029/RG027i003p00329

Grose MR et al (2020) Insights from CMIP6 for Australia's future climate. Geophys Res Lett 8:5. https://doi.org/10.1029/2019EF001469

Haarsma RJ, Roberts MJ, Vidale PL, Senior CA, Bellucci A, Bao Q, Chang P, Corti S, Fučkar NS, Guemas V, von Hardenberg J, Hazeleger W, Kodama C, Koenigk T, Leung LR, Lu J, Luo J-J, Mao J, Mizielinski MS, Mizuta R, Nobre P, Satoh M, Scoccimarro E, Semmler T, Small J, von Storch J-S (2016) High Resolution Model Intercomparison Project (HighResMIP v1.0) for CMIP6. Geosci Model Dev 9:4185–4208. https://doi.org/10.5194/gmd-9-4185-2016

Haidvogel DB, Arango HG, Hedstrom K, Beckmann A, Malanotte-Rizzoli P, Shchepetkin AF (2000) Model evaluation experiments in the North Atlantic Basin: simulations in nonlinear terrain-following coordinates. Dyn Atmos Oceans 32(3):239–281. https://doi.org/10.1016/S0377-0265(00)00049-X

Harrison M, Meindl CF (2001) A statistical relationship between El Niño-Southern Oscillation and Florida wildfire occurrence. Phys Geogr 22(3):187–203. https://doi.org/10.1080/02723646.2001.10642737

He X, Kim H, Kirstetter PE, Yoshimura K, Chang E-C, Ferguson CR, Erlingis JM, Hong Y, Oki T (2015) The diurnal cycle of precipitation in regional spectral model simulations over West Africa: sensitivities to resolution and cumulus schemes. Wea Forecast 30(2):424–445. https://doi.org/10.1175/WAF-D-14-00013.1

Huffman GJ, Bolvin DT, Nelkin EJ, Tan J (2019) Integrated multi-satellite retrievals for GPM (IMERG) technical documentation. https://gpm.nasa.gov/sites/default/files/document_files/IMERG_doc_190909.pdf

Juang HM, Kanamitsu M (1994) The NMC nested regional spectral model. Mon Wea Rev 122:3–26. https://doi.org/10.1175/1520-0493(1994)122%3c0003:TNNRSM%3e2.0.CO;2

Kanamaru H, Kanamitsu M (2007) Scale-selective bias correction in a downscaling of global analysis using a regional model. Mon Weather Rev 135:334–350. https://doi.org/10.1175/MWR3294.1

Kerr RA (2011) Vital details of global warming are eluding forecasters. Science 334(6053):173–174. https://doi.org/10.1126/science.334.6053.173

Klein SA, Soden BJ, Lau N-C (1999) Remote sea surface temperature variations during ENSO: Evidence for a tropical atmospheric bridge. J Clim 12:917–932

Laprise R (2014) Comment on 'The added value to global model projections of climate change by dynamical downscaling: A case study over the continental US using the GISS-ModelE2 and WRF models' by Racherla et al. J Geophys Res Atmos 119(7):3877–3881. https://doi.org/10.1002/2013JD019945.2012

Lau N-C, Nath MJ (1996) The role of the atmospheric bridge in linking tropical Pacific ENSO events to extratropical SST anomalies. J Clim 9:2036–2057

Li H, Kanamitsu M, Hong SY (2012) California reanalysis downscaling at 10 km using an ocean-atmosphere coupled regional model system. J Geophys Res Atmos 117:D12. https://doi.org/10.1029/2011JD017372

Li H, Kanamitsu M, Hong SY, Yoshimura K, Cayan DR, Misra V (2014a) A high-resolution ocean-atmosphere coupled downscaling of the present climate over California. Clim Dyn 42(3–4):701–714. https://doi.org/10.1007/s00382-013-1670-7

Li H, Kanamitsu M, Hong SY, Yoshimura K, Cayan DR, Misra V, Sun L (2014b) Projected climate change scenario over California by a regional ocean-atmosphere coupled model system. Clim Change 122(4):609–619. https://doi.org/10.1007/s10584-013-1025-8

Liang-Liang Li, Jiang L, Ru-Cong Y (2022) Evaluation of CMIP6 HighResMIP models in simulating precipitation over Central Asia. Adv Clim Chang Res 13:1–13. https://doi.org/10.1016/j.accre.2021.09.009

Loschnigg J, Webster PJ (2000) A coupled ocean-atmosphere system of SST modulation for the Indian Ocean. J Clim 13:3342–3360

Misra V, Mishra A (2016) The oceanic influence on the rainy season of Peninsular Florida. J Geophys Res Atmos 121(13):7691–7709. https://doi.org/10.1002/2016JD024824

Misra V, Dirmeyer PA, Kirtman BP (2001) Regional simulation of interannual variability over South America. J Geophys Res. https://doi.org/10.1029/2001JD900216

Misra V, Mishra A, Li H (2016) The sensitivity of the regional coupled ocean-atmosphere simulations over the Intra-Americas seas to the prescribed bathymetry. Dyn Atmos Oceans 76:29–51. https://doi.org/10.1016/j.dynatmoce.2016.08.007

Misra V, Mishra A, Bhardwaj A (2019) A coupled ocean-atmosphere downscaled climate projection for the peninsular Florida region. J Mar Syst 194:25–40. https://doi.org/10.1016/j.jmarsys.2019.02.010

Moorthi S, Suarez MJ (1992) Relaxed Arakawa-Schubert A parameterization of moist convection for general circulation models. Mon Weather Rev 120(6):978–1002. https://doi.org/10.1175/1520-0493(1992)120<0978:RASAPO>2.0.CO;2

Palmer TN (2014) Build high-resolution global climate models. Nature 515:338–339. https://doi.org/10.1038/515338a

Pielke RA Sr, Wilby RL (2012) Regional climate downscaling: what's the point? Eos 93:52–53

Putrasahan DA, Kamenkovich I, Henaff LM, Kirtman BP (2017) Importance of ocean mesoscale variability for air-sea interactions in the Gulf of Mexico. Geophys Res Lett.https://doi.org/10.1002/2017GL072884

Racherla PN, Shindell DT, Faluvegi GS (2012) The added value to global model projections of climate change by dynamical downscaling: a case study over the continental US using the GISS-ModelE2 and WRF models. J Geophys Res Atmos 117:1984–2012. https://doi.org/10.1029/2012JD018091

Roads J (2004) Experimental weekly to seasonal U. S. forecasts with the regional spectral model. Bull Am Soc 85:1888–1902. https://doi.org/10.1175/BAMS-85-12-1887

Seager R, Naik N, Vecchi GA (2010) Thermodynamic and dynamic mechanisms for large-scale changes in the hydrological cycle in response to global warming. J Clim 23:4651–4668. https://doi.org/10.1175/2010JCLI3655.1

Shchepetkin AF, McWilliams JC (2005) The regional oceanic modeling system (ROMS): a split-explicit, free-surface, topography-following-coordinate oceanic model. Ocean Model 9(4):347–404. https://doi.org/10.1016/j.ocemod.2004.08.002

Siqueira L, Kirtman BP (2016) Atlantic near-term climate variability and the role of a resolved Gulf Stream. Geophys Res Lett 43:3964–3972

Tiedtke M (1983) The sensitivity of the time-mean large-scale flow to cumulus convection in the ECMWF model. In: Proceedings of ECMWF workshop on convective in large-scale models. European Centre for Medium-Range Weather Forecasts, Reading, United Kingdom, pp 297–316. https://www.ecmwf.int/node/12733

Trenberth KE, Guillemot CJ (1995) Evaluation of the global atmospheric moisture budget as seen from analyses. J Clim 8:2255–2272. https://doi.org/10.1175/1520-0442(1995)008%3c2255:EOTGAM%3e2.0.CO;2

Virgilio GD, Evans JP, Di Luca A, Grose MR, Round V, Thatcher M (2020) Realised added value in dynamic downscaling of Australian climate change. Clim Dyn 54:4675–4692

von Storch J-S (2000) Signature of air-sea interactions in a coupled atmosphere-ocean GCM. J Clim 13:3361–3379

Wang B, Ding Q, Fu X, Kang I-S, Jin K, Shukla J, Doblas-Reyes F (2005) Fundamental challenge in simulation and prediction of summer monsoon rainfall. Geophys Res Lett 32:L15711. https://doi.org/10.1029/2005GL022734

Webster P (2006) The coupled monsoon system. In: Wang B (ed) The Asian Monsoon. Springer, Heidelberg, pp 3–66

Wu R, Kirtman BP, Pegion K (2006) Local air-sea relationship in observations and model simulations. J Clim 19:4914–4932. https://doi.org/10.1175/JCLI3904.1

Wu R, Kirtman BP, Pegion K (2008) Local rainfall-SST relationship on sub-seasonal time scales in satellite observations and CFS. Geophys Res Lett 35:L22706. https://doi.org/10.1029/2008GL035883

Zhang L, Xu Y, Meng CC, Li X, Wang CG (2020) Comparison of statistical and dynamic downscaling techniques in generating high-resolution temperatures in China from CMIP5 GCMs. J App Meteorol. https://doi.org/10.1175/JAMC-D-19-0048.1

Zhao Q, Carr FH (1997) A prognostic cloud scheme for operational NWP models. Mon Weather Rev 125(8):1931–1953. https://doi.org/10.1175/1520-0493(1997)125%3c1931:APCSFO%3e2.0.CO;2